Open Ceramics 17 (2024) 100555

Contents lists available at ScienceDirect

Open Ceramics

journal homepage: www.sciencedirect.com/journal/open-ceramics

Properties and antibacterial activity of $MnFe_2O_4$ nanoparticles obtained by pulsed laser ablation in liquid

S. Özçelik [a], [**], B. Özçelik [b], B. Arıkan [c], S. Kocamaz [c], H. Amaveda [d], L.A. Angurel [d], [*], G.F. de la Fuente [d]

[a] Hakkari University, Engineering Faculty, Food Engineering Department, 30000, Hakkari, Turkey
[b] Cukurova University, Faculty of Science&Letters, Dept. of Physics, 01330, Adana, Turkey
[c] Cukurova University, Faculty of Science&Letters, Dept. of Biology, 01330, Adana, Turkey
[d] Instituto de Nanociencia y Materiales de Aragón, INMA (CSIC-University of Zaragoza), 50018, Zaragoza, Spain

ARTICLE INFO

Handling Editor: P Colombo

Keywords:
$MnFe_2O_4$ spinel
Pulsed laser ablation
Antibacterial activity

ABSTRACT

In this study, $MnFe_2O_4$ nanoparticles (NPs) were fabricated via pulsed laser ablation in liquid. Chemical and structural composition, microstructure, magnetic and antibacterial properties were characterized. Spinel was found as the main crystalline phase, while Fe_2O_3 and Mn_2O_3 were observed as the major secondary phases, all identified by X-ray diffractometry (XRD). Observation by Transmission Electron Microscopy (TEM) indicated that most of the nanoparticles were spherical in shape and found in agglomerates, most likely because of their magnetic nature. Moreover, Fast Fourier Transform of selective area electron diffraction patterns pointed at the existence of crystalline particles. The coercive field (H_c) and saturation magnetization (M_s) values determined for these NPs were found to increase with decreasing temperature. Their antibacterial properties were evaluated using the viable bacteria counting technique (colony) for $MnFe_2O_4$ concentrations of 100 and 300 μg/mL with *Bacillus subtilis*, *Salmonella typhimurium*, *Pseudomonas aeruginosa*, *Klebsiella pneumoniae* and *Escherichia coli* strains.

1. Introduction

Interest in nanoparticles has been on the rise for the last several decades because of their unique physical properties and their potential applications in the optics and electronic engineering and biomedical areas, among others [1]. Particular attention has been given to nano-sized spinel ferrites because of their attractive properties and excellent photostability, high quantum yield and high surface/volume ratio [2]. They are thus relevant for applications in rechargeable lithium batteries [3], chemical and biological sensors [3], catalysis [4], microwave absorbers [5], high-density data storage and magnetic media [6], gas sensors [7], nano-antibiotic therapy [8], imaging and medical applications [9], capping agents to deliver payloads (fertilizers, agrochemicals) into a specific location of fruit trees or high-input crops [6,10], non-invasive cell tracking [11], labelling, stimulating stem cells [12], ferro-fluids [13], monitoring in-vitro/in-vivo behavior [14,15], and cancer diagnosis [16].

Iron based spinel ferrites are represented by the formula MFe_2O_4 (M = Ni, Mn, Zn, Co, Cu, Mg, Cd) and exhibit a face-centered cubic structure with a space group Fd3m. In the general crystallographic representation of the spinel structure, the oxygen anions distribute in a cubic close-packed array in which M^{2+} and Fe^{3+} cations locate in tetrahedral and octahedral lattice sites. The cubic unit cell is constituted by 56 atoms, including 32 oxygen anions situated in the cubic close-packed structure and 24 cations occupying 8 of the 64 convenient tetrahedral M sites and 16 of the 32 available octahedral Fe sites. According to the position of the cations, the structure is described as normal or inverse spinel [17].

Recently, the microorganism resistance to antibiotic treatments has become a reason for concern, because of potential harmful effects on human health. For example, increasing formation of genes with higher resistance to antibiotics has in recent years been observed in definite bacteria contacting with humans and animals [18]. It has been reported that the immunity of certain microorganisms against any pathogen is due to indiscriminate use of antibiotics and is even more serious when it causes side effects reflecting increased bacterial resistance to many antibiotics [19].

---

[*] Corresponding author.
[**] Corresponding author.
E-mail addresses: sezenozcelik@hakkari.edu.tr (S. Özçelik), angurel@unizar.es (L.A. Angurel).

https://doi.org/10.1016/j.oceram.2024.100555
Received 23 October 2023; Received in revised form 4 February 2024; Accepted 19 February 2024
Available online 21 February 2024

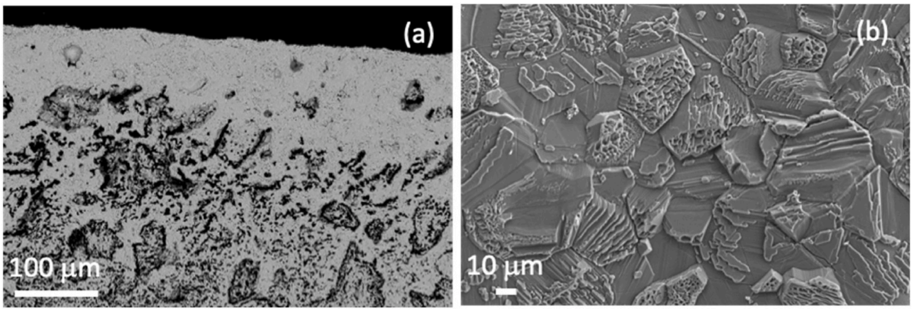

Fig. 1. (a) Aspect of the cross-section of the target sample after laser furnace treatment. (b) FESEM image of the as-solidified Laser Furnace (LF) sample surface.

Given the necessity to find new options for the control of bacterial and fungal spreads in uncontrolled environments, very limited studies have been reported using concepts related to the interaction of nanostructured materials and microorganisms and examining the possible effects of such contacts [20–23].

In recent years and because of their potential for very broad technological applications, many studies have been performed on the production of spinel ferrite nanoparticles. For synthesizing spinel ferrite powders at the nanoscale, very common techniques such as sol–gel coprecipitation [24], hydrothermal [25,26], template-assisted sol–gel [27], in situ catalytic decomposition of benzene over nanoparticles methods [28] have been explored and reported.

All these techniques generally pose several disadvantages. These include the presence of very large particles and non-uniform size distribution, containing impurities that prevent further improvement in the performance of the products [29]. The development of new spinel ferrites synthesis methods which provide lower environmental and health hazards and avoid the use of solvents and expensive precursor materials is therefore of current interest.

The Laser Zone Melting (LZM) method [30–34] can be used as a densification process for most metal oxides at high solidification rates. It was thus chosen for this study to produce dense $MnFe_2O_4$ pellets at high speeds. These were subsequently used as targets to fabricate nanoparticles by a pulsed laser ablation method in liquid. In this context, the purpose of the present study is to evaluate the physical and magnetic properties of the laser produced $MnFe_2O_4$ nanoparticles using XRD, SEM, TEM, and magnetometry. In addition, their antibacterial activity was studied using Salmonella typhimurium (S. typhimurium), Pseudomonas aeruginosa (P. aeruginosa), Bacillus subtilis (B. subtilis), Escherichia coli (E. coli) and Klebsiella pneumoniae (K. pneumoniae) strains.

2. Experimental procedures

2.1. Fabrication of the $MnFe_2O_4$ target

To fabricate the manganese ferrite spinel ($MnFe_2O_4$) target sample, stoichiometric amounts of MnO (Sigma-Aldrich, 99.8%, $d < 10$ µm) and Fe_2O_3 (IROX-00T-500, 95–98%, H_2O solubility $<1\%$ Phosphate (PO_4) $<0.3\%$, Manganese (Mn) $< 0.25\%$, Sulfates (SO_4) $<0.5\%$, $d < 1$ µm) were weighted and ball milled 30 min at 300 rpm in distilled water. By heating with infrared lamps, the water was evaporated from the resulting slurries. After drying, the resulting powders were manually milled and then pressed into a pellet with a thickness of 3 mm and a diameter of 20 mm.

A Laser Zone Melting (LZM) process was performed using a Laser Furnace (LF) apparatus [35]. Laser treatment was performed with the sample inside a 4 m-long roller furnace (Nanetti, model ER) using a transverse rate of 1500 mm/h. The sample temperature passed through a hot zone with a maximum furnace temperature of 1000 °C. A 350 W CO_2 laser system (Rofin-Sinar Slab-type, UK) operating in pulsed mode with a 20 kHz repetition frequency and a 50 µs pulse duration was employed as source emitting under a 40% duty cycle. The laser beam scanned the sample surface at 15875 mm/s. This configuration transforms the circular cross-section of the beam (0.8 mm in diameter) into a 70 mm long line, while the sample is moved in the perpendicular direction with a 544 lines/mm filling factor.

Fig. 1 shows the aspect of the cross section and the surface of the target sample. During the laser process, temperatures higher than 1500 °C were reached at the sample surface. This indicates that MnO and Fe_2O_3 grains have undergone either through a melting, followed by directional solidification, particularly near the irradiated surface, or through a liquid-phase sintering process [36–38]. The cross-section presented in Fig. 1(a) confirms that the laser treatment was able to generate a layer of dense, resolidified material with a thickness ranging

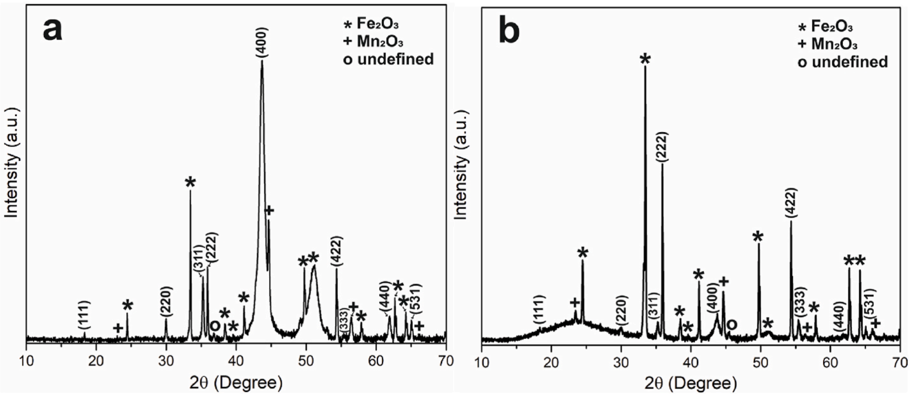

Fig. 2. XRD patterns obtained (a) on the bulk Laser Furnace $MnFe_2O_4$ spinel target and (b) on representative nanoparticles obtained by pulsed laser ablation in liquid, as described in the text.

between 60 and 120 µm. EDS analysis within this region suggests an Fe/Mn at% composition ratio of ca. 2.05, consistent with the formation of the spinel compound. Below this outer layer, the laser output energy was not sufficient to obtain a uniform liquid phase. Fig. 1(b) shows the aspect of the surface where the resolidified $MnFe_2O_4$ grains exhibit a laminar microstructure and seem to appear within a dense solidified liquid matrix. In fact, their microstructure suggests a growth component out of the solidification plane, in line with a significant contribution from cooling rates at the sample's surface, as compared to those imposed by the sample transverse rate in the orthogonal direction of forced solidification [30,34]. XRD pattern of the surface target has been measured with a "PANalytical Model: EMPYREAN" diffractometer by using CuKα radiation in the range $2\theta = 10\text{-}70^\circ$. Results presented on Fig. 2 (a), conforming, as it is going to be explained in section 3.1, that a crystalline $MnFe_2O_4$ phase is formed during the LZM process, with a preferential orientation that is reflected with the high intensity of the line associated with the (400) plane.

2.2. *Fabrication and characterization of $MnFe_2O_4$ nanoparticles*

$MnFe_2O_4$ nanoparticles have been produced using a pulsed laser ablation in liquid (distilled water) technique described in a previous study with a 800 ps n-IR pulsed laser (Rofin-Sinar) [39]. X-ray diffraction patterns have been measured with the same equipment used to characterize the target. Size distribution and electron diffraction patterns of the laser synthesized nanoparticles were obtained by Transmission Electron Microscopy (TEM). Initial studies were performed in a T20 (FEI TECNAI T20) microscope and additional ones in a high resolution uncorrected F30 (FEI TECNAI F30) apparatus, where imaging studies were combined with EDX in STEM mode. Magnetic hysteresis measurements were carried out in a Lake Shore model 7304 Vibrating Sample Magnetometer, operating within the 15–300 K temperature range.

The antibacterial activity of the nanoparticles ($MnFe_2O_4$) was analyzed using the viable bacteria counting technique (colony). Bacterial strains were isolated from patients in different units treated in the intensive care unit of Çukurova University Faculty of Medicine. Bacteria used in antimicrobial activity tests were identified with the vitek-2 system with an accuracy of 98%. Müller Hilton broth and agar were used as medium for antibacterial activity tests using the following bacterial strains: the Gram-positive *Bacillus subtilis*, and the Gram-negative ones: *Salmonella typhimurium*, *Pseudomonas aeruginosa*, *Klebsiella pneumoniae* and *Escherichia coli*.

For the antibacterial activity test, $MnFe_2O_4$ nanoparticles were added to Müller Hilton broth at 100 and 300 µg/mL concentrations. Test bacteria were grown overnight in LB broth and 100 µL inoculated into Müller Hilton broth containing 100 and 300 µg/mL $MnFe_2O_4$ nanoparticles. As a control, 100 µL was inoculated into 1 mL of Müller Hilton broth medium without nanoparticles [40]. Control and test samples were incubated overnight at 37 °C. After an incubation period, 10^6 dilution control and test organisms are inoculated using the spreading technique on Müller Hilton agar. This application was performed in three replications for each sample. Colonies of control and test bacteria grown on the media were counted. The average of the colony numbers obtained from control petri dishes (three petri dishes) was taken and accepted as reference. The average values were found by counting the colonies obtained from the test bacterial strains. The antibacterial effect was determined by proportioning the colony numbers obtained from the control and the 100 and 300 µg/mL $MnFe_2O_4$ containing media.

3. Results and discussions

3.1. *Structure analysis*

As can be seen in Fig. 2, the structure composition of the initial $MnFe_2O_4$ target and of the fabricated nanoparticles was analyzed using XRD patterns. In the case of nanoparticles, the most intense diffraction lines correspond to the (222) and (422) planes, according to PDF Card No.:00-002-1392 Quality:0. These are associated to a cubic structure with space group *Fd3m*. The lattice parameter $\boldsymbol{a}$ and the volume of the unit cell $\boldsymbol{V}$ were calculated using:

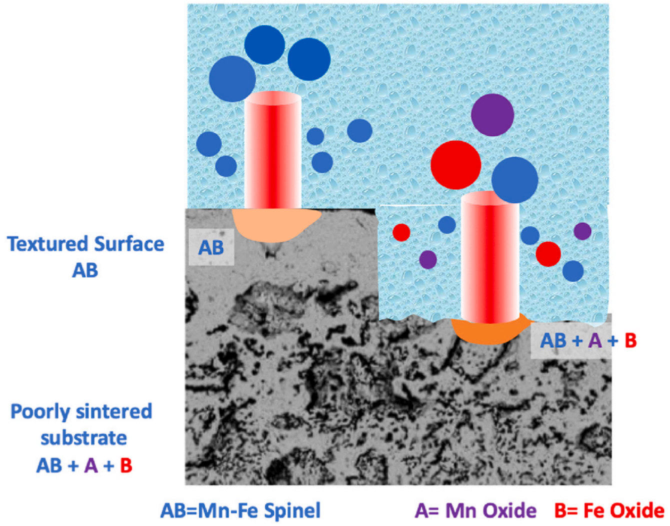

Fig. 3. Scheme of different steps of the ablation process observed when the laser process has affected several regions of the substrate.

$$\frac{1}{d^2}=\frac{h^2+k^2+l^2}{\boldsymbol{a}^2}, V=a^3$$

in which $\boldsymbol{d}$ is the distance between planes in the atomic lattice and the h, k, l are Miller indices. The calculated $\boldsymbol{a}$ and $\boldsymbol{V}$ values are 8.52 (±0.01) Å and 618.47 $Å^3$, respectively. These obtained values are in good agreement with the crystallographic cell dimensions in bulk and nanoparticles of $MnFe_2O_4$ [41]. Moreover, as a general feature of nanomaterials, some reflections such as (220), (311), (400), (333), (440) and (531) are weaker and broader than those observed in the corresponding bulk form. In addition, there are also several secondary diffraction lines associated mainly with Fe_2O_3 (*) and also with Mn_2O_3 (+) phases. These could indicate a complex ablation process involving several phenomena occurring simultaneously. On the one hand, it may indicate that ablation has not been confined to the external part of the target surface, where the spinel phase was synthesized during the Laser furnace process, and, in consequence, nanoparticles have also been generated via ablation when the laser has reached the less-densified granular material below this outer, dense surface and the three phases (spinel, iron oxide and manganese oxide) are still present (Fig. 3).

The fact that melting takes place during the ablation process is supported by the observation of spherical particles, formed by surface tension during the ejection of liquid droplets from the melt, a typical phenomenon observed during ns laser ablation. In addition, it is important to consider that molten volume is affected by a gradient of irradiance levels associated to the gaussian energy distribution within the laser beam cross section. This would generate differences in viscosity within the melt, resulting in smaller and larger droplets and particles emanating from the irradiated laser spot.

The former arguments are also consistent with the following ones, provided by recent comprehensive studies from published pulsed laser ablation in liquid studies [39]. For example, Amendola et al. [42] review the synthesis of nanoparticles in liquid and describe several extreme phenomena, as, for instance, melting and evaporation or fusion of NPs to form larger ones. In the latter case, if NPs fuse, they resolidify rapidly giving way to new NPs with probably less structural order (line broadening) and potential segregation of phases (spinel transforming partially into its constituent oxides, for example), as could be deduced from work

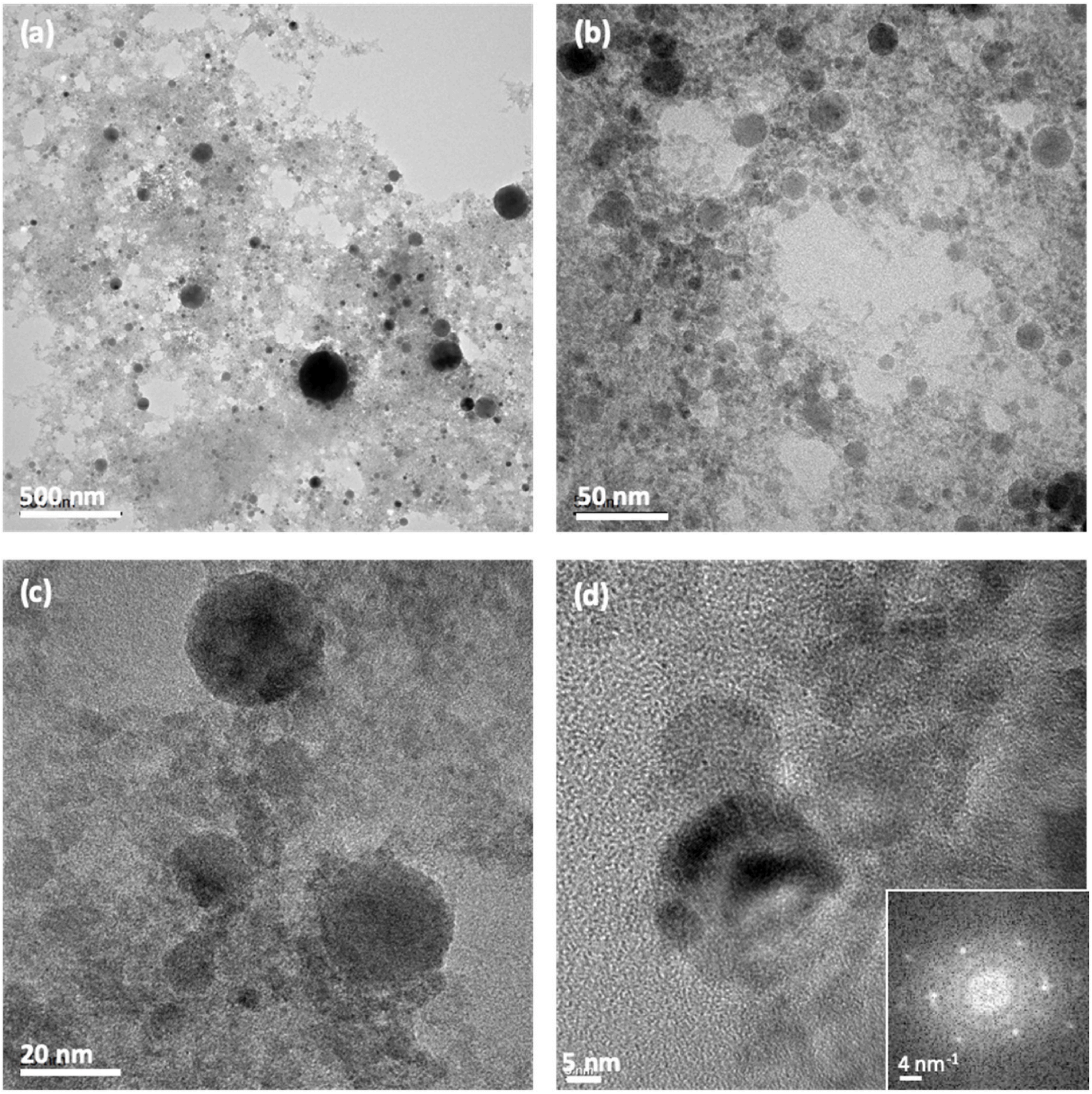

Fig. 4. TEM images for different magnifications of $MnFe_2O_4$ nanoparticles. Inset presented in (***d***) shows the Fast Fourier Transform of selective area electron diffraction pattern obtained on a representative particle.

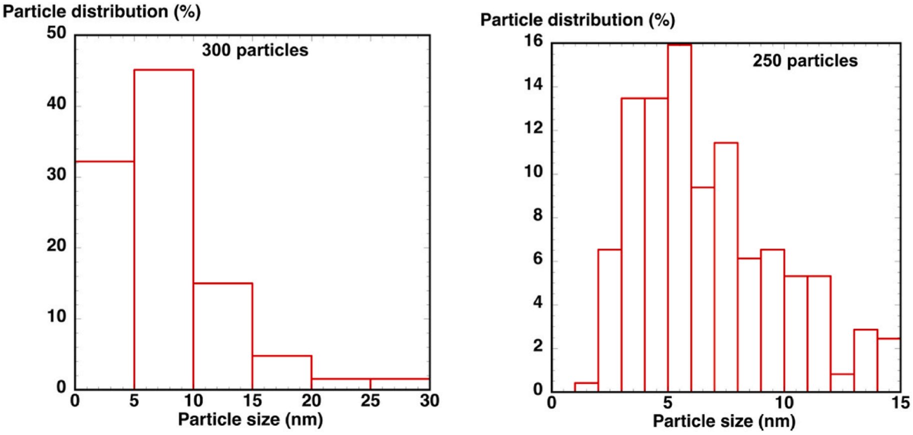

Fig. 5. Particle size distribution of the nanoparticles observed by TEM and shown, in part, in Fig. 4.

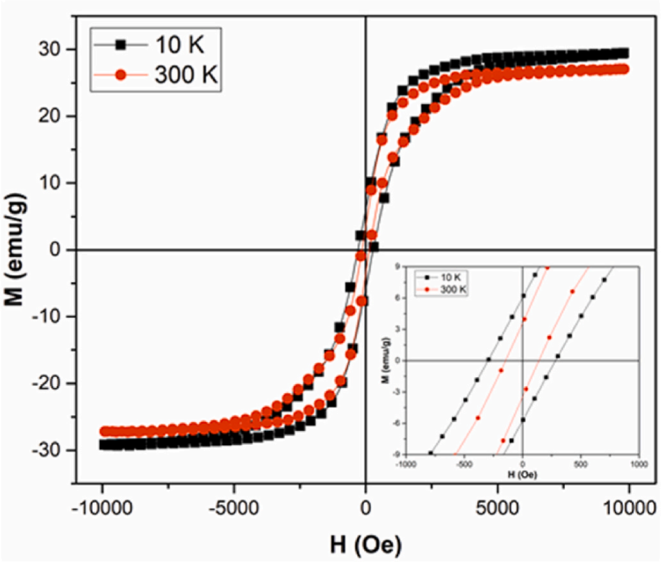

Fig. 6. *M-H* curves obtained on representative $MnFe_2O_4$ nanoparticle at T = 300 K and 10 K. The inset shows the enlarged hysteresis loop within the range ±800 Oe.

reporting on a Mn–Fe–O phase equilibria revisiting study [36].

3.2. Morphological study

Representative TEM micrographs obtained on nanoparticles prepared by *n*-IR 800 ps Laser Ablation of $MnFe_2O_4$ are presented in Fig. 4. The four micrographs were recorded at different magnification, with size scale bars ranging between 500 nm and 5 nm, as labeled in each micrograph. From these images, it is apparent that most of the nanoparticles are spherical in shape, arising from a molten phase, as discussed earlier, and with significant agglomeration due to their magnetic nature [39,43]. Moreover, the Fast Fourier Transform of selective area electron diffraction patterns, given in the inset of Fig. 4(d), constitute distinctive, continuous spotty circles pointing out the existence of crystalline particles with regular lattice spacings.

The size distribution of the $MnFe_2O_4$ nanoparticles is given in Fig. 5, where a significant fraction is observed to fall within the 1–15 nm size range. Additionally, many nanoparticles with size below 10 nm are observed throughout the samples. Moreover, few spherical nanoparticles with diameters higher than 20 nm are observed as a minority fraction and their appearance is likely produced by shock wave-induced ejection of droplets from the thin melt layer formed during irradiation of the target surface [44,45]. They may also be a consequence of prolonged thermalization of the plasma plume confined in a cavitation bubble [46], via reflected shock waves during sustained oscillatory expansion and contraction of its volume [47]. To produce nanoparticles from a solid $MnFe_2O_4$ target at a pulse duration of 800 ps and a near-IR irradiation wavelength, laser ablation may involve several simultaneous mechanistic pathways. These are not clearly defined in the literature related to Pulsed Laser Ablation in Liquids (PLAL), as are those ranging within ultrashort (tens to hundreds of fs) and short (tens to hundreds of ns) pulses, reviewed in detail [48,49]. It can be argued that the direct sublimation arising from the solid surface under sub-ns pulsed irradiation may yield very small diameter particles [41,43], as this phenomenon occurs within a very short time, following each pulse irradiation and before a dominant electron-phonon relaxation mechanism becomes significant. The particle size distribution may thus be expected, with the largest fraction in the small nanometer size range, with a very minor fraction of larger nanoparticles. This is consistent with the observations reported in the above TEM observations, where a monomodal distribution appears to be characteristic.

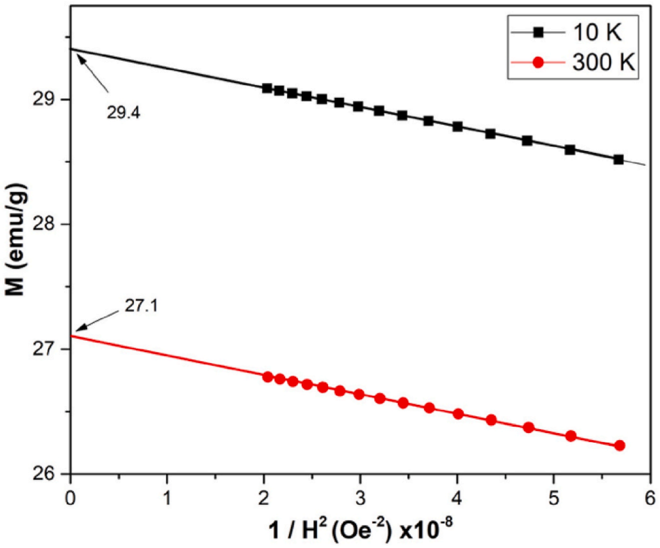

Fig. 7. Plots of *M* vs $1/H^2$ obtained on representative $MnFe_2O_4$ nanoparticles at T = 300 K and 10 K.

3.3. Magnetic properties

In order to monitor the magnetic nature of $MnFe_2O_4$ nanoparticles produced via pulsed laser ablation in water, magnetic hysteresis measurements were performed within a ±10 kOe range at 10 and 300 K, respectively. The results are presented in Fig. 6, and it may be concluded that the hysteresis curves exhibit a very narrow *S*-shape behaviour. This is a clear indication and evidence for a soft ferromagnetic behaviour, which increases with increasing magnetic field up to an intrinsic saturation value. The remanent magnetization (M_r) and coercivity field (H_c) values of $MnFe_2O_4$ nanoparticles measured at 10 and 300 K were determined as 5.9 and 3.44 emu/g for $\mathbf{M_r}$ and 284.5 and 142.3 Oe for $\mathbf{H_c}$, respectively. The field dependence of the magnetization (*M*) near its saturation value is given by Ref. [50]:

$$M = M_s\left[1 - \frac{\beta}{H^2}\right]$$

where M_s is the saturation magnetization, β is a parameter related to anisotropy including magneto-crystalline anisotropy, shape anisotropy, etc. and *H* is the applied magnetic field. As can be seen in Fig. 7, M_s and β values at 10 and 300 K can be obtained by plotting *M* versus $1/H^2$, from both, the slope of the linear fitting and the interception with the y-axis, respectively. The values thus obtained are 29.4 and 27.1 emu/g for M_s and 1.56×10^7 and 1.50×10^7 Oe^2 for β, respectively. If the β value is found, the magnetic anisotropy constant (K_a) can be conveniently calculated using the equation below [50]:

$$K_a = M_s\sqrt{\frac{15\beta}{4}}$$

The deduced K_a values at 10 and 300 K are 2.25×10^5 and 2.03×10^5 erg/g, respectively.

Finally, it can be argued that the increase of magnetic quantities, saturation magnetization, coercivity field, remanent magnetization at low temperature is due to the decrease in thermal fluctuations of the magnetic moment. It can be concluded that in these nanoparticles H_c values are smaller, which is evidence of soft ferromagnetic behaviour, and M_s values are slightly lower than those obtained in samples prepared via a thermal decomposition method. But the general behaviour of these magnetic magnitudes agrees with those found in the literature [41,43].

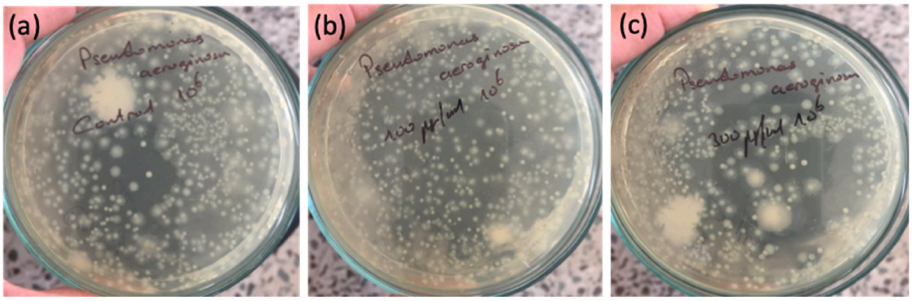

Fig. 8. Antibacterial effect of $MnFe_2O_4$ nanoparticles in *Pseudomonas aeruginosa*. (a) Control sample, (b) 100 μg/mL $MnFe_2O_4$ containing media; and (c) 300 μg/mL $MnFe_2O_4$ containing media.

Table 1
Antibacterial effect of $MnFe_2O_4$ nanoparticles in *Bacillus subtilis* and Gram negative *Enterobacteriaceae* strains. The antibacterial effect has been measured as the percentage of reduction in the number of viable colonies.

Bacteria	$MnFe_2O_4$ (100 μg/mL) Antibacterial Effect %	$MnFe_2O_4$ (300 μg/mL) Antibacterial Effect %
Bacillus subtilis	51.82 ± 0.92	71.13 ± 0.94
Salmonella typhimurium	51.22 ± 0.83	68.19 ± 1.72
Pseudomonas aeruginosa	8.83 ± 0.85	43.11 ± 1.05
Klebsiella pneumonia	52.74 ± 0.83	65.04 ± 0.90
Escherichia coli	58.03 ± 1.20	82.05 ± 1.05

3.4. Antibacterial properties

The antibacterial activity of the synthesized $MnFe_2O_4$ nanoparticles was analyzed using the live bacteria counting technique (colony). For this purpose, the number of bacteria colonies grown in test media prepared with nanoparticles at different concentrations have been compared with the number that grow in a control medium. The reduction in the number of colonies measured in the test media has been evaluated as the percentage of antibacterial effect. As an example, the antibacterial activity observed with *Pseudomonas aeruginosa* is presented in Fig. 8. In the case of this strain, the concentration of $MnFe_2O_4$ has a great importance. For low concentration values, 100 μg/mL, the antibacterial effect only reaches an 8.8%, a value that increases up to 43.1% when the concentration is 300 μg/mL. It is possible that the biofilm layer synthesized by the *Pseudomonas aeruginosa* strain [51–53] prevents the entry of $MnFe_2O_4$ into the bacteria. It is also important to mention that the appearance of apparent contamination in the Petri dishes is due to the use of strains isolated directly from the patient in the antimicrobial activity test.

As can be observed in Table I, the synthesized nanoparticles exhibited antibacterial effect in all the strains that have been used in this work: *Bacillus subtilis*, *Salmonella typhimurium, Pseudomonas aeruginosa, Klebsiella pneumoniae* and *Escherichia coli*. When the 100 μg/mL concentration is used, the antibacterial activity reaches percentages of 51.87%, 51.22%, 8.83%, 52.74% and 58.03%, respectively. On the other hand, when the concentration increases to 300 μg/mL, these percentages increase until 71.13%, 68.19%, 43.11%, 65.04% and 82.05% for each type of analyzed bacteria. S.K. Jesudoss et al. [54] have investigated the antibacterial activity of spinel $Mn_{1-x}Ni_xFe_2O_4$ nanoparticles synthesized via microwave combustion method, against two Gram positive bacteria (*S. aureus* and *B. subtilis*) and two Gram negative bacteria (*P. aeruginosa* and *E. coli*) isolated at the concentration of 200 μg/mL. They have observed the higher antibacterial activities for $x = 0.5$ composition, reaching values of 24.1% and 18.4% for *S. aureus* and *B. subtilis* and 20.5% and 15.5% for *P. aeruginosa* and *E. coli*, respectively. In comparison with this study, the nanoparticles prepared in this work exhibit higher antibacterial activities for each examined bacterium. As it is well-known, in general, the antibacterial efficiency of spinel ferrite nanoparticles strongly depends on their particle size, surface area and morphology. It can be argued that pulsed laser ablation in liquid for the fabrication of spinel nanoparticles plays a very positive role towards their biological applications.

4. Conclusions

The present study reports on the antibacterial activity of $MnFe_2O_4$ nanoparticles (NPs). Dense solid targets were fabricated using a laser zone melting process within a patented Laser Furnace device at temperatures close to 1000 °C. Nanoparticles were subsequently produced using a pulsed laser ablation in liquid method with a 800 ps n-IR laser source, irradiating the Laser Furnace produced, stoichiometrically corresponding dense blank, submerged in distilled water. The following results may be highlighted.

- TEM observations show that most of the nanoparticles were spherical in shape, indicating that they were produced after melting in the ablation process. In addition, they exhibit significant agglomeration due to their magnetic nature.
- The size distribution of the $MnFe_2O_4$ nanoparticles was determined to be largely within the 1–15 nm range.
- XRD measurements show that a high level of crystallinity was reached in the fabricated nanoparticles. This is consistent with FFT analysis of selective area electron diffraction patterns that shows continuous, spotty circles pointing out the existence of crystalline nanoparticles.
- The remanent magnetization (M_r) and coercivity field (H_c) values of these nanoparticles were determined at 10 and 300 K, as 5.9 and 3.44 emu/g for $\mathbf{M_r}$ and 284.5 and 142.3 Oe for $\mathbf{H_c}$, respectively.
- The synthesized nanoparticles exhibited an important antibacterial activity, that depends on the nanoparticle concentration, both with Gram-positive and Gram-negative test bacteria strains. The highest antibacterial effect was obtained in *Escherichia coli*, a value that reaches 58.03% for 100 μg/mL and 82.05% for 300 μg/mL. The lowest effect was observed when working with *Pseudomonas aeruginosa* strain, where also a strong influence on the nanoparticles concentration was observed. In the other three strains, antibacterial activities of the order of 65–71% have been reached, when a particle concentration of 300 μg/mL was used.

Declaration of competing interest

The authors declare that they have no known competing financial interests or personal relationships that could have appeared to influence the work reported in this paper.

Acknowledgements

B. O. acknowledges the Scientific and Technological Research Council of Turkey (TUBITAK) for a grant via 2219-Science Fellowships and Grant Programs Department, with the project number: 1059B192000390. The authors gratefully acknowledge the financial support from the Spanish MCIN/AEI/10.13039/501100011033 (project PID2020-113034RB-I00) and from Gobierno de Aragón (research group T54_23R). Authors also would like to acknowledge the use of Servicio General de Apoyo a la Investigación-SAI and ICTS ELECMI, nodo "Laboratorio de Microscopías Avanzadas (LMA), Universidad de Zaragoza.

References

[1] G.C. Hadjipanaysis, Magnetic hysteresis in novel magnetic materials, in: NATO ASI Series: Serie E: Applied Sciences, vol. 338, Springer Netherlands, 1997, 9780792346043.

[2] G. Kandasamy, K. Kumar, Synergy between nanoparticles and breast cancer theranostics, in: N.D. Thotat, J. Bauer (Eds.), Nanomedicines for Breast Cancer Theranostics, Elsevier, Amsterdam, 2020, pp. 71–106, https://doi.org/10.1016/B978-0-12-820016-2.00005-7.

[3] K. Thanigai Arul, M. Elayaperumal, R. Ladchumananandasivam, M. Maaza, Novel PVA polymer based nanostructure with ferrites co-doped with nickel and cobalt ions for Magneto-Sensor application, Polym. Int. 65 (2016) 1482–1485, https://doi.org/10.1002/pi.5242.

[4] K.S. Lin, A.K. Adhikari, Z.Y. Tsai, Y.P. Chen, T.T. Chien, H.B. Tsai, Synthesis and characterization of nickel ferrite nanocatalysts for CO_2 decomposition, Catal. Today 174 (2011) 88–96, https://doi.org/10.1016/j.cattod.2011.02.013.

[5] S. Tyagi, H.B. Baskey, R.C. Agarwala, V. Agarwala, T.C. Shami, Development of hard/soft ferrite nanocomposite for enhanced microwave absorption, Ceram. Int. 37 (2011) 2631–2641, https://doi.org/10.1016/j.ceramint.2011.04.012.

[6] A.H. Latham, E. Williams, Controlling transport and chemical functionality of magnetic nanoparticles, Acc. Chem. Res. 41 (2008) 411–420, https://doi.org/10.1021/ar700183b.

[7] N. Dogan, A. Bingolbali, L. Arda, D. Akcan, Synthesis, structure, and magnetic properties of $Ni_{1-x}Zn_xFe_2O^4$ nanoparticles, J. Supercond. Nov. Magnetism 30 (2017) 3611–3617, https://doi.org/10.1007/s10948-016-3899-y.

[8] K. Elayakumar, A. Manikandan, A. Dinesh, K. Thanrasu, K.K. Raja, R.T. Kumar, Y. Slimani, S.K. Jaganathan, A. Baykal, Enhanced magnetic property and antibacterial biomedical activity of Ce^{3+} doped $CuFe_2O_4$ spinel nanoparticles synthesized by sol-gel method, J. Magn. Magn Mater. 478 (2019) 140–147, https://doi.org/10.1016/j.jmmm.2019.01.108.

[9] S. Lee, S. Bae, Y. Takemura, E. Yamashita, J. Kunisaki, C. Kim, Magnetic properties, self-temperature rising characteristics, and biocompatibility of $NiFe_2O_4$ nanoparticles for hyperthermia applications, IEEE Trans. Magn. 42 (2006) 2833–2835, https://doi.org/10.1109/INTMAG.2006.375636.

[10] A. Tomitaka, A. Hirukawa, T. Yamada, S. Morishita, Y. Takemura, Biocompatibility of various ferrite nanoparticles evaluated by in vitro cytotoxicity assays using HeLa cells, J. Magn. Magn Mater. 321 (2009) 1482–1484, https://doi.org/10.1016/j.jmmm.2009.02.058.

[11] T. Tomitaka, M. Jeun, S. Bae, Y. Takemura, Evaluation of magnetic and thermal properties of ferrite nanoparticles for biomedical applications, J. Magnet 16 (2011) 164–168, https://doi.org/10.4283/JMAG.2011.16.2.164.

[12] J. Singh, A. Roychoudhury, M. Srivastava, V. Chaudhary, R. Prasanna, D.W. Lee, S. H. Lee, B.D. Malhotra, Highly efficient bienzyme functionalized biocompatible nanostructured nickel Ferrite-Chitosan nanocomposite platform for biomedical application, J. Phys. Chem. C 117 (2013) 8491–8502, https://doi.org/10.1021/jp312698g.

[13] M.M.L. Sonia, S. Anand, S. Blessi, S. Pauline, A. Manikandan, Effect of surfactants (PVB/EDTA/CTAB) assisted sol-gel synthesis on structural, magnetic and dielectric properties of $NiFe_2O_4$ nanoparticles, Ceram. Int. 44 (2018) 22068–22079, https://doi.org/10.1016/j.ceramint.2018.08.317.

[14] C.X. Guo, S. Huang, X. Lu, A solventless thermolysis route to large-scale production of ultra-small hydrophilic and biocompatible magnetic ferrite nanocrystals and their application for efficient protein enrichment, Green Chem. 16 (2014) 2571–2579, https://doi.org/10.1039/C3GC42645A.

[15] E. Leal, J. Dantas, P.T.A. dos Santos, S.M.C.M. Bicalho, R.H.G.A. Kiminami, M.R. da Silva, A.C.F.M. Costa, Effect of the surface treatment on the structural, morphological, magnetic and biological properties of MFe_2O_4 iron spinels (M=Cu, Ni, Co, Mn and Fe) Appl, Surf. Sci. 455 (2018) 635–645, https://doi.org/10.1016/j.apsusc.2018.06.025.

[16] Ç.E. Demirci Dönmez, P.K. Manna, R. Nickel, S. Aktürk, J. van Lierop, Comparative heating efficiency of cobalt-, manganese-, and nickel- ferrite nanoparticles for a hyperthermia agent in biomedicines, ACS Appl. Mater. Interfaces 11 (2019) 6858–6866, https://doi.org/10.1021/acsami.8b22600.

[17] J. Smit, H.P.J. Wijn, Ferrites. Philips Technical Library, Cleaver- Home Press Ltd, The Netherlands, 1959.

[18] World Health Organization, Antimicrobial Resistance: Global Report on Surveillance, WHO Press, Geneva, Switzerland, 2014.

[19] M. Raffi, S. Mehrwan, T.M. Bhatti, J.I. Akhter, A. Hameed, W. Yawar, M.M. Hasan, Investigations into the bacterial behavior of copper nanoparticles against Escherichia coli, Ann. Microbiol. 60 (2010) 75–80, https://doi.org/10.1007/s13213-010-0015-6.

[20] M. Hundáková, K. Dedková, G.S. Martynková, Decoration of inorganic substrates with metallic nanoparticles and their application as antimicrobial agents, in: M. Rai, R. Shegokar (Eds.), Metal Nanoparticles in Pharma, Springer Cham, 2017, pp. 295–336.

[21] L. Lin, H. Cui, G. Zeng, M. Chen, H. Zhang, M. Xu, X. Shen, C. Bortolini, M. Dong, Ag-$CuFe_2O_4$ magnetic hollow fibers for recyclable antibacterial materials, J. Mater. Chem. B 1 (2013) 2719–2723, https://doi.org/10.1039/C3TB20223B.

[22] S. Xavier, H. Cleetus, P.J. Nimila, S. Thankachan, R.M. Sebastian, E. M. Mohammed, Structural and antibacterial properties of silver substituted cobalt ferrite nanoparticles, Res. J. Pharmaceut. Biol. Chem. 5 (2014) 364–371.

[23] P. Gong, H. Li, X. He, K. Wang, J. Hu, W. Tan, Z. Shouchun, X. Yang, Preparation and antibacterial activity of Fe_3O_4@Ag nanoparticles, Nanotechnology 18 (2007) 285604, https://doi.org/10.1088/0957-4484/18/28/285604.

[24] M.B. Tahir, T. Iqbal, A. Hassan, S. Ghazal, Wet chemical co- precipitation synthesis of nickel ferrite nanoparticles and their characterization, J. Inorg. Organomet. Polym. 27 (2017) 1430–1438, https://doi.org/10.1007/s10904-017-0598-5.

[25] J. Huo, M. Wei, Characterization and magnetic properties of nanocrystalline nickel ferrite synthesized by hydrothermal method, Mater. Let. 63 (2009) 1183–1184, https://doi.org/10.1016/j.matlet.2009.02.024.

[26] H. Li, H.Z. Wu, G.X. Xiao, Effects of synthetic conditions on particle size and magnetic properties of $NiFe_2O_4$, Powder Technol. 198 (2010) 157–166, https://doi.org/10.1016/j.powtec.2009.11.005.

[27] D.Y. Li, Y.K. Sun, P.Z. Gao, X.L. Zhang, H.L. Ge, Structural and magnetic properties of nickel ferrite nanoparticles synthesized via a template-assisted sol–gel method, Ceram. Int. 40 (2014) 16529–16534, https://doi.org/10.1016/j.ceramint.2014.08.006.

[28] M. Parishani, M. Nadafan, Z. Dehghani, R. Malekfar, G.H.H. Khorrami, Optical and dielectric properties of $NiFe_2O_4$ nanoparticles under different synthesized temperature, Results Phys. 7 (2017) 3619–3623, https://doi.org/10.1016/j.rinp.2017.09.049.

[29] Y.M.Z. Ahmed, Synthesis of manganese ferrite from non-standard raw materials using ceramic technique, Ceram. Intern. 36 (2010) 969–977, https://doi.org/10.1016/j.ceramint.2009.11.020.

[30] V. Lennikov, B. Özkurt, L.A. Angurel, A. Sotelo, B. Özçelik, G.F. de la Fuente, Microstructure and transport properties of Bi-2212 prepared by CO_2 laser line scanning, J. Supercond. Nov. Magn. 26 (2013) 947–952, https://doi.org/10.1007/s10948-012-1934-1.

[31] A. Larrea, G.F. de la Fuente, R.I. Merino, V. Orera, ZrO_2-Al_2O_3 eutectic plates produced by laser zone melting, J. Eur. Ceram. Soc. 22 (2002) 191–198, https://doi.org/10.1016/S0955-2219(01)00279-5.

[32] M. Mora, V.V. Lennikov, H. Amaveda, L.A. Angurel, G.F. de la Fuente, M.T. Bona, C. Mayoral C, J.M. Andrés, J. Sánchez-Herencia, Fabrication of superconducting coatings on structural ceramic tiles, IEEE Trans. Appl. Supercond. 19 (2009) 3041–3044, https://doi.org/10.1109/TASC.2009.2017851.

[33] I. de Francisco, V.V. Lennikov, J.A. Bea, A. Vegas, J.B. Carda, G.F. de la Fuente, In-situ laser synthesis of rare earth aluminate coatings in the system Ln-Al-O (Ln=Y, Gd), Solid State Sci. 13 (2011) 1813–1819, https://doi.org/10.1016/j.solidstatesciences.2011.07.013.

[34] B. Özçelik, S. Özçelik, H. Amaveda, H. Santos, C.J. Borrell, R. Sáez-Puche, G.F. de la Fuente, L.A. Angurel, High speed processing of $NiFe_2O_4$ spinel using a Laser Furnace, J. Materiomics 6 (2020) 661–670, https://doi.org/10.1016/j.jmat.2020.05.003.

[35] L.C. Estepa, G.F. de la Fuente, Continuous furnace with coupled laser for the surface treatment of materials, US Patent 20090230105 (2009) EP1992445 (2008), Continuous Method for the Surface Treatment of Materials, China patent No. ZL 2012100224412. Filing date: March 6, 2007, Published date: March 26, 2014.

[36] J.V. Crum, B.J. Riley, J.D. Vienna, Binary phase diagram of the manganese oxide-iron oxide system, J. Am. Ceram. Soc. 92 (2009) 2378–2384, https://doi.org/10.1111/j.1551-2916.2009.03230.x.

[37] S.J.K. Kang, Part VI: basis of liquid phase sintering in sintering: densification, grain growth, and microstructure, Elsevier Butterworth-Heinemann (2005) 199–203. ISBN: 978-0-7506-6385-4.

[38] R.M. German, P. Suri, S.J. Park, Review: liquid phase sintering, J. Mater. Sci. 44 (2009) 1–39, https://doi.org/10.1007/s10853-008-3008-0.

[39] S. Özçelik, B. Yalçın, L. Arda, H. Santos, R. Sáez-Puche, L.A. Angurel, G.F. de la Fuente, B. Özçelik, Structure, magnetic, photocatalytic and blood compatibility studies of nickel nanoferrites prepared by laser ablation technique in distilled water, J. Alloys Comp. 854 (2021) 157279, https://doi.org/10.1016/j.jallcom.2020.157279.

[40] E. Microbiologischenhandbuch, Merck Darmstadt, 1978.

[41] B. Aslibeiki, P. Kameli, M.H. Ehsani, $MnFe_2O_4$ bulk, nanoparticles and film: a comparative study of structural and magnetic properties, Ceram. Inter 42 (2016) 12789–12795, https://doi.org/10.1016/j.ceramint.2016.05.041.

[42] V. Amendola, D. Amans, Y. Ishikawa, N. Koshizaki, S. Scirè, G. Compagnini, S. Reichenberger, S. Barcikowski, Room-temperature laser synthesis in liquid of oxide, metal-oxide core-shells, and doped oxide nanoparticles, Chem. Eur J. 26 (2020) 9206–9242, https://doi.org/10.1002/chem.202000686.

[43] B. Aslibeiki, Nanostructural, magnetic and electrical properties of Ag doped Mn-ferrite nanoparticles, Current App. Phys. 14 (2014) 1659–1664, https://doi.org/10.1016/j.cap.2014.09.025.

[44] E.T. Itina, On nanoparticle formation by laser ablation in liquids, J. Phys. Chem. C 115 (2011) 5044–5048, https://doi.org/10.1021/jp1090944.

[45] V. Amendola, M. Meneghetti, What controls the composition and the structure of nanomaterials generated by laser ablation in liquid solution? Phys. Chem. Chem. Phys. 15 (2013) 3027–3046, https://doi.org/10.1039/C2CP42895D.

[46] K. Choudhury, R.K. Singh, P. Kumar, M. Ranjan, A. Srivastava, A. Kumar, Effect of confined geometry on the size distribution of nanoparticles produced by laser ablation in liquid medium, Nano-Structures & Nano-Objects 17 (2019) 129–137, https://doi.org/10.1016/j.nanoso.2018.12.006.

[47] T.T.P. Nguyen, R. Tanabe-Yamagishi, Y. Ito, Effects of liquid depth on the expansion and collapse of a hemispherical cavitation bubble induced in nanosecond pulsed laser ablation of a solid in liquid, Opt Laser. Eng. 126 (2020) 105937, https://doi.org/10.1016/j.optlaseng.2019.105937.

[48] A. Kanitz, M.R. Kalus, E.L. Gurevich, A. Ostendorf, S. Barcikowski, D. Amans, Review on experimental and theoretical investigations of the early stage, femtoseconds to microseconds processes during laser ablation in liquid-phase for the synthesis of colloidal nanoparticles, Plasma Sources Sci. Technol. 28 (2019) 103001, https://doi.org/10.1088/1361-6595/ab3dbe.

[49] C.Y. Shih, R. Streubel, J. Heberle, A. Letzel, M.V. Shugaev, C. Wu, M. Schmidt, B. Gökce, S. Barcikowski, L.V. Zhigilei, Two mechanims of nanoparticle generation in picosecond laser ablation in liquids: the origin of the bimodal size distribution, Nanoscale 10 (2018) 6900–6910, https://doi.org/10.1039/C7NR08614H.

[50] H.C. Fang, Z. Yang, C.K. Ong, Y. Li, C.S. Wang, Preparation and magnetic properties of (Zn-Sn) substituted barium hexaferrite nanoparticles for magnetic recording, J. Magn. Magn Mater. 187 (1998) 129–135, https://doi.org/10.1016/S0304-8853(98)00139-5.

[51] S. Kocamaz, D. Kocamaz, B. Arikan, Antibacterial Effect of a bioactive molecule against nosocomial infection agent Escherichia coli isolated from Cukuroca University hospital, Fresenius Environ. Bull. 29 (2020) 4526–4534.

[52] E. Kamali, A. Ardebili, F. Ezadi, A. Mohebbi, Evaluation of antimicrobial resistance, bioflm forming potential, and the presence of bioflm-related genes among clinical isolates of Pseudomonas aeruginosa, BMC Res. Notes 13 (2020) 27, https://doi.org/10.1186/s13104-020-4890-z.

[53] F.P. Tuon, L.R. Dantas, P.H. Suss, V.S.T. Ribeiro, Pathogenesis of the Pseudomonas aeruginosa biofilm: a review, Pathogens 11 (2022) 300, https://doi.org/10.3390/pathogens11030300.

[54] S.K. Jesudoss, J.J. Vijaya, L.J. Kennedy, P.I. Rajan, H.A. Al-Lohedan, R. J. Ramalingam, K. Kaviyarasu, M. Bououdina, Studies on the efficient dual performance of $Mn_{1-x}Ni_xFe_2O_4$ spinel nanoparticles in photodegradation and antibacterial activity, J. Photochemistry & Photobiology, B: Biology 165 (2016) 121–132, https://doi.org/10.1016/j.jphotobiol.2016.10.004.